







## Article

# Evaluation of the Pitting Corrosion of Modified Martensitic Stainless Steel in CO<sub>2</sub> Environment Using Point Defect Model

Ahmed Bahgat Radwan <sup>1</sup>, Abdraman M. Moussa <sup>2</sup>, Noora H. Al-Qahtani <sup>1</sup>, Raymundo Case <sup>3</sup>,  
Homero Castaneda <sup>3</sup>, Aboubakr M. Abdullah <sup>1</sup>, Muhsen A. M. El-Haddad <sup>4</sup>, Jolly Bhadra <sup>1,2</sup>  
and Noora Jabor Al-Thani <sup>2,\*</sup>

- <sup>1</sup> Center for Advanced Materials, Qatar University, Doha P.O. Box 2713, Qatar; ahmedbahgat@qu.edu.qa (A.B.R.); noora.alqahtani@qu.edu.qa (N.H.A.-Q.); bakr@qu.edu.qa (A.M.A.); jollybhadra@qu.edu.qa (J.B.)
- <sup>2</sup> Qatar University Young Scientist Center (QUYSC), Qatar University, Doha P.O. Box 2713, Qatar; abdraman@qu.edu.qa
- <sup>3</sup> Department of Materials Science and Engineering, Texas A&M University, College Station, TX 77843, USA; raymundo.case@tamu.edu (R.C.); hcastaneda@tamu.edu (H.C.)
- <sup>4</sup> Qatargas Operating Company Limited, Doha P.O. Box 22666, Qatar; Melhaddad@qatargas.com.qa
- \* Correspondence: n.al-thani@qu.edu.qa



**Citation:** Radwan, A.B.; Moussa, A.M.; Al-Qahtani, N.H.; Case, R.; Castaneda, H.; Abdullah, A.M.; El-Haddad, M.A.M.; Bhadra, J.; Al-Thani, N.J. Evaluation of the Pitting Corrosion of Modified Martensitic Stainless Steel in CO<sub>2</sub> Environment Using Point Defect Model. *Metals* **2022**, *12*, 233. <https://doi.org/10.3390/met12020233>

**Academic Editors:** Andronikos Balaskas, Youngsik Kim and Santiago Fajardo

Received: 14 December 2021

Accepted: 20 January 2022

Published: 26 January 2022

**Publisher's Note:** MDPI stays neutral with regard to jurisdictional claims in published maps and institutional affiliations.



**Copyright:** © 2022 by the authors. Licensee MDPI, Basel, Switzerland. This article is an open access article distributed under the terms and conditions of the Creative Commons Attribution (CC BY) license (<https://creativecommons.org/licenses/by/4.0/>).

**Abstract:** Pitting corrosion is a significant concern for the broader application of stainless steel in modern industries in which metal and metal alloy are detached preferentially from susceptible parts on the surface, resulting in the creation of holes in passivated alloys that are exposed to an aqueous, neutral electrolyte containing corrosive species. Exposure of SS to brines leads to the localized loss of surface passivity and the onset of isolated pitting, which render the equipment or piping unfit for service. In the present study, the passive layer behavior and the pitting corrosion of the modified martensitic stainless steel (MMSS) were evaluated in a saturated CO<sub>2</sub> environment (pH~5) with different NaCl concentrations and temperatures, using various electrochemical techniques. It was found that by increasing the temperature up to 60 °C, the corrosion resistance of the MMSS increased; however, the corrosion rate dramatically increased at 80 °C, indicating the destruction of the oxide layer. According to the point defect model (PDM) results, the calculated values of polarizability ( $\alpha$ ), metal cation diffusivity ( $D$ ), and the rate of annihilation of cation vacancies ( $j_m$ ), reveal a strong dependence on the solution temperature.

**Keywords:** corrosion; martensitic stainless steel; point defect model; cation vacancies; pitting

## 1. Introduction

Of all forms of corrosion, pitting corrosion is probably the most insidious corrosion, since it concentrates on a tiny area of the materials and often leads to severe failures without any prior indication. Stainless steels are iron alloys containing at least 11% chromium and nickel. Their degradation resistance is accredited to the presence of thin film, identified by the “passive film”, which protects the steel from corrosion and gives rise to its name. There are three types of stainless steels according to their metallurgical structure: body-centered cubic (ferritic), face-centered cubic (austenitic), and body-centered tetragonal or cubic (martensitic).

Martensitic stainless steels are widely used in several industries, exhibiting a high corrosion resistance in the atmosphere and some acidic and alkaline solutions. Nevertheless, they are subjected to localized corrosion problems, such as pitting corrosion, stress corrosion cracking (SCC), and intergranular corrosion [1,2]. Pitting corrosion is widely encountered for most stainless steel, and therefore, significant research has been aimed at determining the mechanism of pitting and developing effective protection methods. Cl<sup>-</sup> induced pitting corrosion of some metal and metal alloys is a spontaneous phenomenon

resulting from the action of hydrated  $\text{Cl}^-$  concentrations and temperature, as well as the composition, type, and microstructural features of the alloy material. Although there are still controversies about the pitting mechanisms, it is generally believed that pitting is initiated through the local breakdown of the barrier layer, owing to the specific interaction of the film and the corrosive ions in the environment [3,4]. Failure of the passive layer occurs at spots on the metal surface distinguished by high cation vacancy diffusivity [5]. These spots contain high disorder in the barrier layer structure at the stainless steel's barrier layer/inclusions interface, such as MnS and other precipitates ( $\text{Cr}_{23}\text{C}_6$ ). Once the destruction of the passive layer exposes the vulnerable base steel, the dissolution of bare metal is confined to this small region, leading to the development of pits with various geometries. The composition and morphology of the protective layer are of great importance in the pitting process. Accordingly, much work has been done to enrich the performance of the bilayer and diminish the susceptibility of stainless steel (SS) to pitting corrosion. Interestingly, Zhang et al. [6] investigated the role of hydrated  $\text{Cl}^-$  ions in the passivity breakdown of a  $\text{FeCr}_{15}\text{Ni}_{15}$  single crystal through a combination of experimental analyses employing spherical Cs-corrected TEM with computational modeling. They proposed that the presence of a particular type of grain boundary between the amorphous region of the passive layer and nanocrystals, NCs, facilitate the ion transport of  $\text{Cl}^-$  to permeate the outer and inner layers and render it undulating and indistinct. The weakest location is envisioned as the critical region for a passivity breakdown that takes place at adjacent places with the influence of subdued  $\text{Cl}^-$  species [6].

On the other hand, the point defect model (PDM) indicates that corrosive halide species, such as bromide (Br), fluoride (F), iodide (I), and chloride (Cl), enter into oxygen vacancies ( $V_{\text{O}}^{\cdot\cdot}$ ) in the barrier film, leading to the construction of cation vacancies  $V_{\text{M}}^{x'}$  at the barrier layer/solution interface (bl/s), and consequently improve the flux of cation vacancies ( $J_{\text{Ca}}$ ) through the passive film in the direction of the metal/barrier layer (m/bl) interface, as demonstrated in Figure 1.

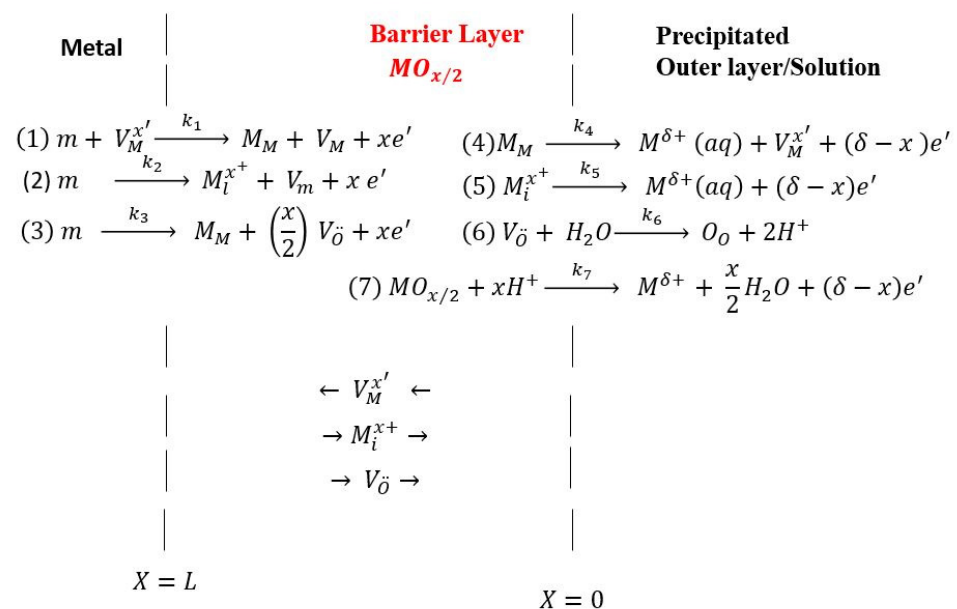


**Figure 1.** Summary of the defect generation and annihilation reactions proposed to take place at the interfaces of the barrier oxide layer on metal, according to the PDM.  $m$  and  $V_{\text{M}}^{x'}$  represent the metal atom and cation vacancy on the cation sublattice of the barrier layer, respectively.  $M_i^{x+}$  is a cation interstitial,  $V_{\text{O}}^{\cdot\cdot}$  is an oxygen (anion) vacancy,  $M^{\delta+}(\text{aq})$  is a cation at the outer layer/solution interface, and  $M_{\text{M}}$  and  $V_{\text{m}}$  are the metal cation on the cation sublattice of the barrier layer and a vacancy in the modified martensitic stainless steel (MMSS) sample, respectively.  $O_{\text{O}}$  is an oxide ion in the anion site on the anion sublattice, and  $MO_{x/2}$  is the stoichiometric barrier layer oxide. Note that the origin of the coordinate system is the bl/s interface, and hence that the flux of oxygen vacancies is negative.

It is worth mentioning that  $j_m$  is the annihilation rate of the  $V_M^{x'}$  at the metal/barrier layer interface (m/bl).  $x$  corresponds to the oxidation number of the host cation within the barrier layer. When  $j_{ca} > j_m$ , the cation vacancies on the cation sublattice of the barrier layer ( $V_M^{x'}$ ) localize at the m/bl interface. Accordingly, at a particular concentration of the cation vacancy, the barrier layer detaches from the base metal, generating a blister from the residual barrier layer. Subsequently, the barrier layer will be disabled from growing into the metal surface, generating  $V_O^{\cdot}$ , as pointed out in the following reaction:

The generated oxygen vacancies  $V_O^{\cdot}$  could autocatalytically react with more  $Cl^-$  species at the bl/electrolyte interface, producing additional oxygen and cation vacancies. The produced cation vacancies could transfer to the MMSS/bl interface and progressively accumulate, giving rise to the separation of the passive layer and the occurrence of breakdown at the most vulnerable locations with the utmost diffusivities for cation vacancies.

In this work, the natural behavior of the passive film of the MMSS was quantitatively evaluated at different temperatures in an electrolyte containing variable contents of chloride, based on the PDM framework. Accordingly, different parameters, such as the diffusivity of the metal cations ( $D$ ), the polarizability of the barrier layer/solution interface ( $\alpha$ ) (i.e., the dependence of the potential drop across the bl/s interface on the applied potential), and the annihilation rate ( $j_m$ ) were calculated to describe the critical factor affecting breakdown potential and to point out the validity of the PDM regime.

## 2. Experimental Section

The MMSS steel specimens were cut from a 230 mm ID tubing with a wall thickness of 18 mm; this tubing is typically used well tubulars. The chemical analysis of the steel is displayed in Table 1.

**Table 1.** Chemical composition of the MMSS steel used in this work (%  $w/w$ ), balance Fe.

C	Si	Mn	P	S	Ni	Cr	Mo
0.01	0.21	0.43	0.017	0.001	5.73	11.91	1.95

Cylindrical samples of about 5 cm in length and 6.3 mm in diameter were cut from the tubing wall. The specimens were polished to a 1200 grit finish before testing, followed by degreasing with acetone.

The electrochemical measurements were performed in a double-jacketed Pyrex glass cell at variable temperatures (20, 40, 60, and 80 °C) in varying concentrations of NaCl (0.1, 1, 10, 35.5 and 100 g/L), employing a Gamry 3000 potentiostat/galvanostat/ZRA (Warminster, PA, USA). The electrolyte pH was adjusted to 5 after purging  $CO_2$  gas (99.99%). All tests were carried out at atmospheric pressure. Prior to any electrochemical test, the specimens were located under open-circuit potential (OCP) conditions for 20 h in the deaerated electrolyte. A Mott–Schottky test was performed at the frequency of 1 kHz in a potential window from  $-1000$  to  $100$  mV Ag/AgCl with an amplitude of 10 mV. The variation in protective film thickness was avoided by applying a scanning rate of 50 mV/step. In all electrochemical tests, a platinum wire (Pt) was employed as a counter electrode and Ag/AgCl (SSC) as a reference electrode. The potentiodynamic polarization plots were attained from  $-0.8$  to  $+0.5$  V versus reference values, at variable scan rates of 0.1, 1, and 10  $mV \cdot s^{-1}$ .

## 3. Results and Discussion

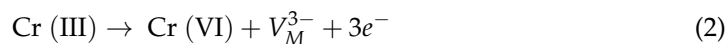
### 3.1. Semiconducting Properties of the Passive Film by Mott–Schottky Analysis

The semiconducting features of the MMSS specimens were evaluated at different concentrations of deaerated NaCl solutions at different temperatures using the Mott–Schottky regime. Figures S1–S5 (Supplementary Materials) exhibit the Mott–Schottky test results of the MMSS samples using variable concentrations of NaCl at different temperatures.

The applied potential and measured space charge capacitance ( $C_{sc}$ ) of the MMSS electrode results in the following formula [7]:

$$\frac{1}{C_{sc}^2} = \pm \frac{2}{e\epsilon\epsilon_0 N_q} \left( E - E_{Fb} - \frac{KT}{e} \right) \quad (1)$$

where the positive sign (+) and negative sign (−) represent the n-type and p-type semiconductor, respectively;  $e$  is the electron charge ( $1.602 \times 10^{-19}$  C);  $\epsilon$  is the dielectric constant for the passive layer, and its value is around 15.6;  $\epsilon_0$  is the vacuum permittivity ( $8.854 \times 10^{-12}$  F·m<sup>−1</sup>);  $N_q$  is the doping density of the donor densities ( $N_D$  for n-type and acceptor densities  $N_A$  for p-type);  $E_{Fb}$  is the flat band potential;  $K$  is the Boltzmann constant ( $1.38 \times 10^{-23}$  J·K<sup>−1</sup>); and  $T$  is the absolute temperature. The calculated values, such as the acceptor density ( $N_A$ ) and donor density ( $N_D$ ), are represented in Table S1 (Supplementary Materials). Figures S1–S5 exhibit the multiple Mott–Schottky regions of the MMSS specimens. This phenomenon was demonstrated by the presence of acceptor/donor states of different energy levels [8–10]. The area with a +Ve slope (−1 to 0.54 V<sub>Ag/AgCl</sub>) is attributed to the n-type semiconductor caused by oxygen vacancies [11,12]. Nonetheless, the −Ve slope region (0.5 to 0 V<sub>Ag/AgCl</sub>) is accredited to the p-type semiconductor, owing to the existence of cation vacancies in the passive layer [12]. It is noteworthy that the passive layer is considered to be n-type if the number of electrons existing in the oxide layer is higher than the number of holes in the valence band, such as TiO<sub>2</sub>, ZnO, MoO<sub>3</sub>, V<sub>2</sub>O<sub>5</sub>, and Fe<sub>2</sub>O<sub>3</sub>. On the other hand, the barrier film is ascribed to be a p-type semiconductor when the number of electrons is less than the number of holes in the valence band of the protective oxide film, such as NiO, Cu<sub>2</sub>O, and Cr<sub>2</sub>O<sub>3</sub> [7]. The metal vacancies content boosted in the barrier layer due to the diminution of Cr (III) in the barrier layer generating a p-type semiconductor, according to the given reaction [13,14]:



It is worth mentioning that the semiconducting performance mirrors the passive film properties composed of the inner region (Cr<sub>2</sub>O<sub>3</sub>) and the outer region (Fe<sub>2</sub>O<sub>3</sub>) at a low concentration of NaCl. Notably, the p-type of the MMSS transformed to an n-type semiconductor at an almost potential ( $E$ ) of 0.386 V<sub>Ag/AgCl</sub> at a higher concentration of NaCl. Hamadou et al. [15] attributed this behavior to the indirect co-relation between defects concentration and semiconducting properties and the capacitance behavior generated from the construction of an inversion film, on account of an increasing hole content in the valence band. On the other hand, Saleh et al. [16] stated that the presence of the n-type in the deep donor state (Fe<sub>2</sub>O<sub>3</sub>) acts as an active site for pitting propagation. Based on the listed results in Table S1, it can be observed that both electron donor ( $N_D$ ) and electron acceptor ( $N_A$ ) values increased by increasing the NaCl concentration, indicating that passive layer instability results in developing the electrochemical reaction at the metal/electrolyte interface due to the improved flux of cation interstitials within the barrier layer [17–19]. Moreover, the high  $N_D$  value indicates the adsorption probability of the chloride species (Cl<sup>−</sup>) into the oxygen vacancies in the passive layer, decreasing the rate of the annihilation of oxygen vacancies at the barrier layer/solution interface (bl/s), i.e.,  $V_o + Cl^- \rightarrow Clo\cdot$ , subsequently increasing the oxygen vacancies rate in the bl and pitting nucleation vulnerability [14]. Thus, the cation interstitial seems to be the likely dominant defect on the MMSS lattice at the passive film/metal interface [20].

### 3.2. Potentiodynamic Polarization

The potentiodynamic polarization was conducted in deaerated electrolytes in different concentrations of NaCl at pH 5 and at different scan rates (see Figures S6–S8 (Supplementary Materials)). Tables S2–S4 (Supplementary Materials) show the derived parameters from the polarized curves, such as the corrosion current density ( $i_{corr}$ ), pitting corrosion ( $E_{pit}$ ), and corrosion potential ( $E_{corr}$ ). It is worth mentioning that the  $i_{corr}$  shifted to more negative

values by increasing the NaCl content. Moreover, the  $E_{pit}$ , which indicates the failure of the barrier layer, negatively shifted to the lower value as the width of the passive region was alleviated at a higher concentration of NaCl. According to the penetration regime suggested by Hoar et al. [21], corrosive anions, such as hydrated  $\text{Cl}^-$  species, penetrate the passive films to the bare metal surface and react specifically with the metal. Based on this idea, Macdonald et al. [22,23] developed a model that attributes the passive film's breakdown to the stress induced by the penetration and accumulation of vacancies at the metal/oxide interface. The authors claimed that the passive film is essentially oxide film with an accumulation of defective points. The development of the barrier film involves the transport of oxygen ions, metals ions, and their vacancies.

Tables S2–S4 (Supplementary Materials) compare the corrosion rate of the MMSS at variable scan rates and high temperatures. The corrosion rate was obtained by employing the following formula:

$$CR = \frac{I_{corr} \cdot K \cdot EW}{dA} \quad (3)$$

where  $CR$  is the corrosion rate in  $\text{mm} \cdot \text{y}^{-1}$ ,  $I_{corr}$  is the corrosion current in amps,  $K$  is the constant that describes the units for the corrosion rate (3272),  $EW$  is the equivalent weight in grams/equivalent,  $d$  is the density in  $\text{grams cm}^{-3}$ , and  $A$  is the sample area in  $\text{cm}^2$ . The  $I_{corr}$  is obtained by extrapolating the fitting lines of the anodic and cathodic branch back to  $E_0$  [24,25].

The corrosion rate was alleviated by increasing the temperature from 20 to 60 °C; however, the CR increased at 80 °C, which could be attributed to the formation of a protective film of the amorphous  $\text{FeCO}_3$  on the MMSS substrate (see Figures S9–S11 (Supplementary Materials)). It is worth noting that the constructed layer is porous and not well-adherent to the steel surface at a temperature below 60 °C [26,27]. Nevertheless, the  $\text{FeCO}_3$  layer becomes denser and adherent to the metal surface, forming a solid passive layer between the metal and the corrosive electrolyte at 60 °C. However, the increasing degradation rate at 80 °C could be ascribed to the higher kinetics of MMSS at different temperatures [26,28]. The presence of iron carbonate hinders the aggressive species from flowing into the oxygen vacancies ( $V_o^\bullet$ ) in the barrier film, leading to the flux of cation vacancies dropping toward m/bl interfaces ( $j_{ca}$ ), reducing the ingress of hydrated  $\text{Cl}^-$  ions. Figure 2 exhibits the formation of hemisphere pits with a diameter of  $\sim 8 \mu\text{m}$  after the potentiodynamic polarization test in 10 g/L NaCl at 20 °C. The elemental distribution of the selected pit was investigated by employing EDS mapping, showing the presence of Fe, Ni, Cr, and Mo after potentiodynamic polarization (see Figure 2). Enriched Mo at the pit mouth can be explained as a result of the construction of  $\text{FeMoO}_4$ , which is more stable at weak acidic conditions (4–6) [29,30].

Figure 3 epitomizes the current transient (i-t) curves extracted from the potentiostatic polarization experiments at variable applied potentials. The current transient nature is related to the onset, growth, and re-passivation of the metastable pits. It is noteworthy that the presence of the fluctuated current transient at a potential lower than  $\text{OCP} + 350 \text{ mV}$  indicates the formation of metastable pitting. The propagation of metastable pits is not controlled by mass transport control, since the calculated current density inside these pits remains constant with time and depends on the applied voltage [31]. In metastable pit growth, the pit evolution is controlled by an ohmic drop across a porous cover on top of the pit. The resistance of the cover is proportional to the inverse power of the pit radius, which explains the constant current density inside the pit. On the other hand, applying a voltage of 350 mV magnitude amplified the pitting current of the stable pit after 580 s, influenced by chemical alterations of the electrolyte inside the pit, giving rise to the persistent pitting development across the exposed MMSS substrate [32]. Once a pit starts to grow, it follows a self-propagating or autocatalytic mechanism [33].

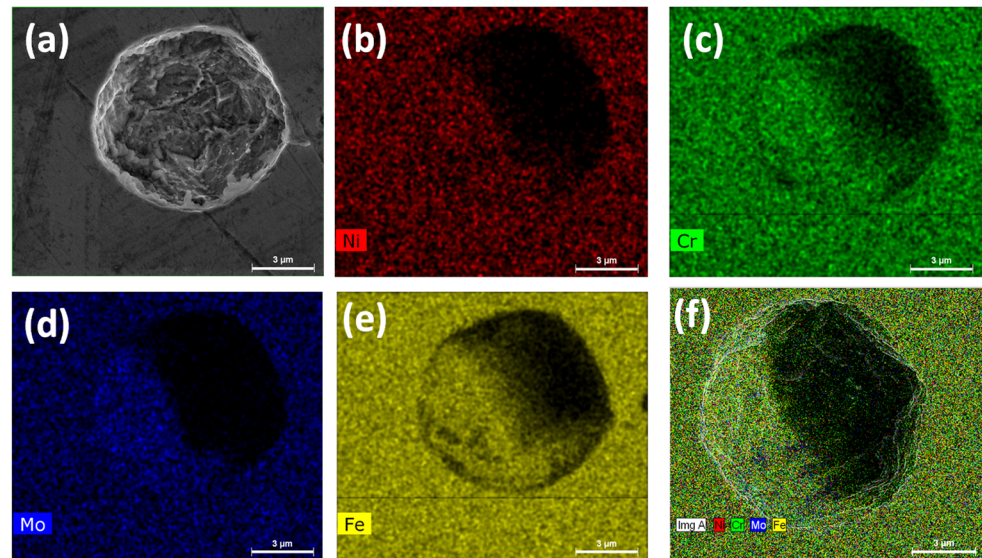


**Figure 2.** SEM image of (a) MMSS after potentiodynamic polarization in 10 g/L NaCl at 20 °C in a saturated CO<sub>2</sub> environment (pH~5), showing a pit formation and the corresponding EDX elemental mapping of (b) Ni, (c) Cr, (d) Mo, (e) Fe and (f) Ni, Cr, Mo, Fe.

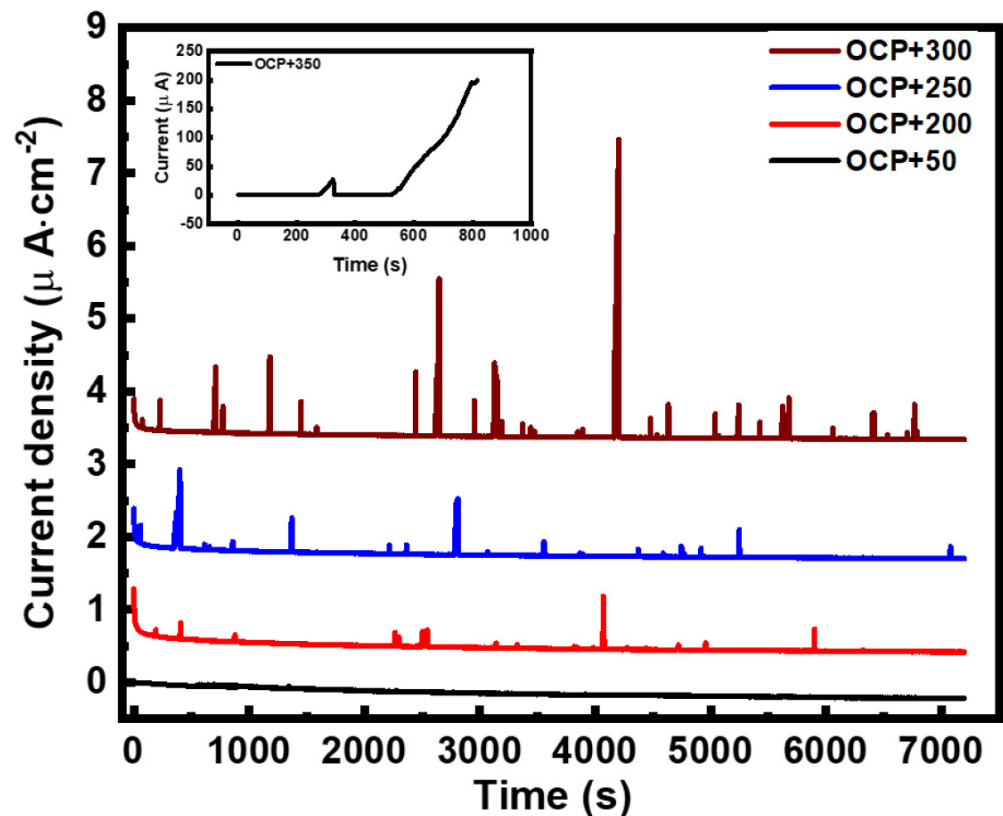


**Figure 3.** Chrono-amperometric curves were obtained from the staircase potentiostatic test carried out on the MMSS steel at 20 °C with 35.5 g/L NaCl in a saturated CO<sub>2</sub> environment (pH~5).

Figure 4 displays the effect of variable NaCl concentrations on the average passive current of the MMSS steel ( $i_{passive}$ ) derived from the potentiostatic results at different temperatures. It is noteworthy that the passive current dwindled until reaching a temperature of 60°. Nevertheless, the current boosted sharply at a lower potential when using high concentrations of NaCl due to the accumulation of the oxygen vacancies fractions at the

bilayer/solution interface, leading to a downward flux of oxygen ions at the MMSS/bilayer interface [34].

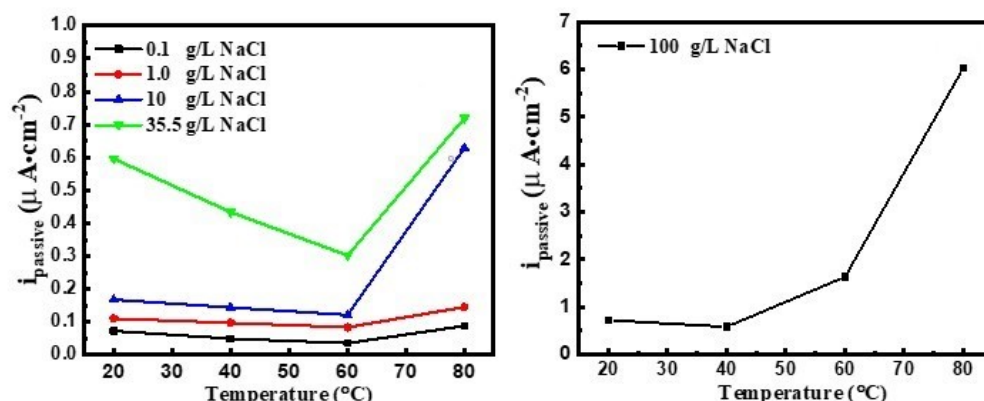


**Figure 4.** The average  $i_{passive}$  values were derived from the potentiostatic experiment using variable concentrations of NaCl at elevated temperatures in a saturated  $\text{CO}_2$  environment (pH~5).

Figures S12–S14 (Supplementary Materials) exhibit the impact of temperature on the  $\alpha$  (the polarizability of the bl/solution interface) values, which were estimated from the linear dependence of the pitting potential ( $V_C$ ) at variable scan rates (0.1, 1, 10 mV/s) on  $\log(a_{Cl^-})$  based on the following equations [35,36]:

$$V_C = \frac{4.606RT}{\chi\alpha F} \log\left(\frac{b}{D}\right) - \frac{2.303RT}{\alpha F} \log(a_{Cl^-}) \quad (4)$$

$$b = \frac{RTJ_m\Omega}{F\chi\epsilon N_v} \cdot \exp\left(\frac{w - \frac{\chi}{2}\beta FpH}{RT}\right) = \frac{RTJ_m\Omega}{F\chi\epsilon N_v} \cdot \exp\left(\frac{\Delta G_s^0 + \frac{\chi}{2}\Delta G_A^0 - \frac{\chi}{2}\beta FpH - \frac{\chi}{2}F\phi_{f/s}^0}{RT}\right) \quad (5)$$

$$\phi_{f/s} = \phi_{f/s}^0 + \alpha V + \beta pH \quad (6)$$

where  $D$  is the diffusivity of the cation vacancy in the barrier layer ( $\text{cm}^{-2}\cdot\text{s}^{-1}$ ), and  $a_{Cl^-}$  is the  $\text{Cl}^-$  species activity. The parameters  $\chi$ ,  $\epsilon$ , and  $\Omega$  are the oxide stoichiometry ( $\text{MO } \chi/2$ ), the electric field strength within the barrier layer, and the volume per mole of cation in the film, respectively.  $\Delta G_s^0$  and  $\Delta G_A^0$  are the change in standard Gibbs energy for the Schottky-pair reaction ( $\text{Null} \xrightarrow{\text{Schottky}} \frac{\chi}{2}V_o^{\cdot\cdot} + V_M^{\cdot\prime}$ ) and for the absorption of the anions into oxygen vacancies at the film/solution interface, respectively [37].  $J_m$  is the annihilation rate of cation vacancies at the metal/film interface. The parameters  $\alpha$  and  $\beta$  are the dependencies of the potential drop through the film/solution interface ( $\phi_{f/s}$ ) on the applied potential  $V$  and pH, respectively.  $\phi_{f/s}^0$  is the value of  $\phi_{f/s}$  in the standard state of  $V = 0$ ,  $R$  is the gas constant,  $T$  is the temperature,  $pH = 0$ ,  $N_v$  is Avogadro's number,  $F$  is Faraday's constant, and  $w$  describes the energy related to the absorption of  $\text{Cl}^-$  ions [37,38].

$$w = \Delta G_s^0 + \frac{\chi}{2}\Delta G_A^0 - \frac{\chi}{2}F\phi_{f/s}^0 \quad (7)$$

The dependency of  $\alpha$  values on the increase in temperature, as listed in Table 2, could be ascribed to the adsorption of  $\text{CO}_3^{2-}$  anions onto the surface of oxygen vacancies, in competition with chloride ions. Accordingly, the electric flux passing into the bl/solution interface is reduced due to the adsorption of  $\text{O}_2^-$  on the oxyanion, which alleviates the +Ve charge at this interface [20].

**Table 2.** The effect of temperature on the polarization value at variable scan rates.

Temperature	0 mV/s	0.1 mV/s	1 mV/s	10 mV/s
20	0.11	0.301	0.283	0.228
40	0.1	0.209	0.220	0.213
60	0.08	0.209	0.196	0.190
80	0.07	0.356	0.267	0.234

Figure 5 displays the pitting potential as a function of variable voltage scan rates at different temperatures, exhibiting a linear dependency and consistency with the PDM. It is worth mentioning that the pitting potential significantly shifted to the more negative values and narrowed the stable passive range at higher concentrations of NaCl due to the growth of the current in the stable passivity, which somewhat decreased the protection effectiveness. The value of the cation annihilation rate at the bl/MMSS interface ( $j_m$ ) was estimated by employing the following formula [37]:

$$V_c(v) = \left( \frac{2\zeta RT}{j_m \chi \alpha} \right)^{\frac{1}{2}} v^{\frac{1}{2}} + V_c(v=0) \quad (8)$$

where  $\zeta$  is the critical areal cation vacancy concentration derived from the crystal structure of the metal oxide, which is presumed to be  $\text{Cr}_2\text{O}_3$  and the corresponding metal substrate, from the values reported in the literature, where  $\zeta = 3.5 \times 10^{14} \text{ cm}^{-2}$  [20].

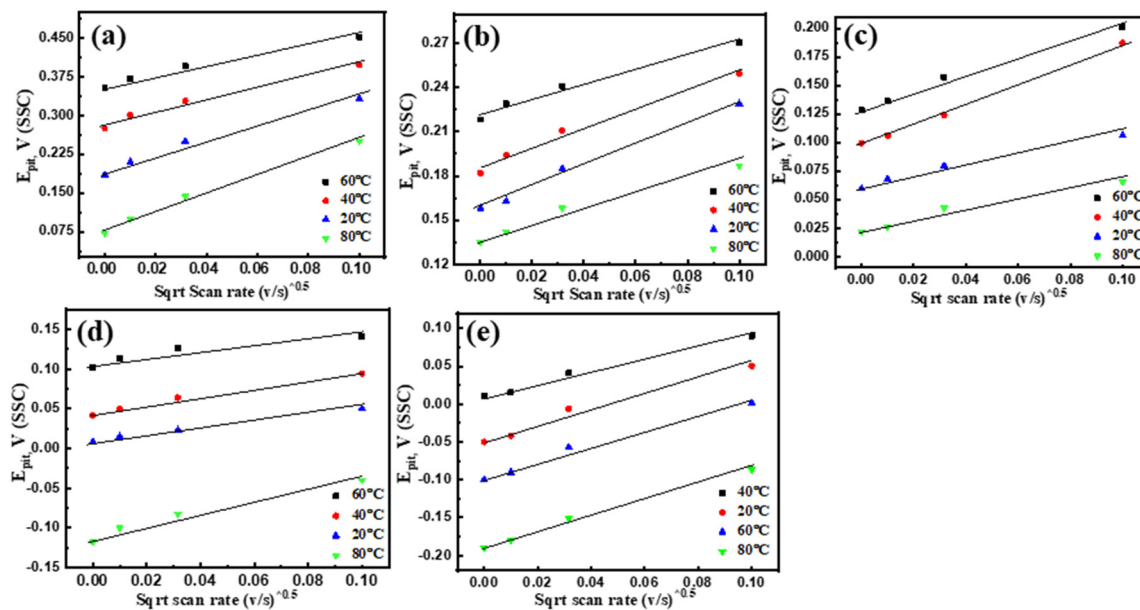


**Figure 5.** Effect of the temperature and the polarization scan rate on the apparent pitting potential of the MMSS steel at different temperatures, using variable concentrations of (a) 0.1, (b) 1 (c) 10, (d) 35.5, and (e)  $100 \text{ g}\cdot\text{L}^{-1}$  of NaCl in a saturated  $\text{CO}_2$  environment (pH~5).

The cation oxidation state ( $\chi$ ) within the bl is supposed to be three, since  $\text{Cr}_2\text{O}_3$  encompasses the inner layer at bl/MMSS surfaces. It is noteworthy that the preferential oxidation of chromium before the onset of Fe oxidation gives rise to considerable growth of  $\text{Cr}_2\text{O}_3$  within the barrier layer [39]. Additionally, the mobility of Cr cations is lower than that of Fe cations in bl lattices, leading to the favorable transmission of Fe cations as metal interstitials. The  $j_m$  values displayed a dependency with decreasing the corrosion rate, indicating that the constructed passive layer becomes protective by increasing the temperature up to  $60^\circ\text{C}$ . The annihilation rate of the cation vacancies could lead to the accumulation of metal vacancies ( $V_M^{\chi'}$ ) on the lattice of the MMSS alloy, as described in Figure 1. Therefore, the barrier layer detaches from the metal/bl interface, giving rise to the initiation of localized corrosion.

The values of the metal cation diffusivity,  $D$ , are attained from Equations (4) and (5), employing the corresponding values of  $\alpha$  and  $j_m$ , and the outcomes are tabulated in Table S5 (Supplementary Materials). It is noteworthy that there is a high density of potential breakdown locations with “weak points” distributed on any real metal surface. Consequently, the distribution of the breakdown locations is represented by the diffusivity of cation vacancies. These places are identified as being regions of high local discontinuity in the barrier layer, such as the points of intersection of the barrier layer with precipitates, inclusions (e.g., MnS), and other “second phase” particles; grain boundaries between nanocrystallites of the barrier layer; and metal dislocations that project through the barrier layer. It is apparent that the  $D$  values possess the similar behavior of the  $\alpha$  and  $j_m$  values ascribed to the construction of a stable passive layer and compact protective film of  $\text{FeCO}_3$  at  $60^\circ\text{C}$ . However,  $D$  values exhibit a dependency with increasing the temperature up to  $80^\circ\text{C}$ , resulting in the destruction



of the passive film and a higher diffusion rate of the cations towards the film/solution interface of the passive layer to interact with the aggressive anion species.

#### 4. Conclusions

The electrochemical behavior of the passive layer of the MMSS samples was evaluated in different concentrations of NaCl at different temperatures. According to the Mott–Schottky test, results show that the cation interstitial seems to be the likely dominant defect on the MMSS lattice at the passive film/metal interface. The corrosion rate decreased by increasing the temperature up to 60 °C due to the formation of the protective layer of FeCO<sub>3</sub>. However, this trend changed by increasing the content of NaCl up to 100 g/L, exhibiting a passivity breakdown at 40 °C. The analysis of the dependence of the breakdown potential on chloride activity resulted in different values of the polarizability ( $\alpha$ ) of the bl/electrolyte interface. The linear relationship between the breakdown potential and chloride activity validated the PDM framework in elucidating the passivity breakdown of MMSS. The diffusivity results of the metal cations ( $D$ ) reveal a similar behavior of  $\alpha$  and  $j_m$ , indicating the passive layer is highly stable at 60 °C. Correlation between experimental data on the breakdown potential ( $E_b$ ) as functions of chloride ion concentration and temperature and different potential scan rates demonstrates the validity of the PDM in analyzing the breakdown behaviors of MMSS.

**Supplementary Materials:** The following supporting information can be downloaded at: <https://www.mdpi.com/article/10.3390/met12020233/s1>, Figure S1: Mott-Schottky plot of 0.1 g/L NaCl at (a) 20 °C, (b) 40 °C, (c) 60 °C and (d) 80 °C in a saturated CO<sub>2</sub> environment (pH~5); Figure S2: Mott-Schottky plot of 1.0 g/L NaCl at (a) 20 °C, (b) 40 °C, (c) 60 °C and (d) 80 °C in a saturated CO<sub>2</sub> environment (pH~5); Figure S3: Mott-Schottky plot of 10 g/L NaCl at (a) 20 °C, (b) 40 °C, (c) 60 °C and (d) 80 °C in a saturated CO<sub>2</sub> environment (pH~5); Figure S4: Mott-Schottky plot of 35.5 g/L NaCl at (a) 20 °C, (b) 40 °C, (c) 60 °C and (d) 80 °C in a saturated CO<sub>2</sub> environment (pH~5); Figure S5: Mott-Schottky plot of 100 g/L NaCl at (a) 20 °C, (b) 40 °C, (c) 60 °C and (d) 80 °C in a saturated CO<sub>2</sub> environment (pH~5); Figure S6: Potentiodynamic polarization plots of MSS for (a) 0.1 g/L, (b) 1 g/L, (c) 10 g/L, (d) 35.5 g/L and (e) 100 g/L of NaCl in a saturated CO<sub>2</sub> environment (pH~5) at scan rate (0.1 mV/s), respectively; Figure S7: Potentiodynamic polarization plots of MSS for (a) 0.1 g/L, (b) 1 g/L, (c) 10 g/L, (d) 35.5 g/L and (e) 100 g/L of NaCl in a saturated CO<sub>2</sub> environment (pH~5) at scan rate (1 mV/s), respectively; Figure S8: Potentiodynamic polarization plots of MSS for (a) 0.1 g/L, (b) 1 g/L, (c) 10 g/L, (d) 35.5 g/L and (e) 100 g/L of NaCl in a saturated CO<sub>2</sub> environment (pH~5) at scan rate (10 mV/s), respectively; Figure S9: The variation of the corrosion rate as a function of (a) different content of NaCl (b) 100 g/L NaCl at elevated temperatures (0.1 mV/s), in a saturated CO<sub>2</sub> environment (pH 5); Figure S10: The variation of the corrosion rate as a function of (a) variable concentrations of NaCl, (b) 100 g/L NaCl at elevated temperatures (1 mV/s) in a saturated CO<sub>2</sub> environment (pH~5); Figure S11: The variation of the corrosion rate as a function of (a) variable concentrations of NaCl, (b) 35.5 and 100 g/L NaCl at elevated temperatures (10 mV/s) in a saturated CO<sub>2</sub> environment (pH~5); Figure S12: The variation of pitting potential as a function of the chloride activity  $a_{Cl}$  at (a) 20 °C, (b) 40 °C, (c) 60 °C and (d) 80 °C, respectively, in a saturated CO<sub>2</sub> environment (pH~5) at a scan rate (0.1 mV/s); Figure S13: The variation of pitting potential as a function of the chloride activity  $a_{Cl}$  at (a) 20 °C, (b) 40 °C, (c) 60 °C and (d) 80 °C, respectively, in a saturated CO<sub>2</sub> environment (pH~5) at scan rate (1 mV/s); Figure S14: The variation of pitting potential as a function of the chloride activity  $a_{Cl}$  at (a) 20 °C, (b) 40 °C, (c) 60 °C and (d) 80 °C, respectively, in a saturated CO<sub>2</sub> environment (pH~5) at scan rate (10 mV/s). Table S1: Donor and acceptor density ( $N_D/N_A$ ) of the oxide films formed on MSS in a saturated CO<sub>2</sub> environment (pH~5); Table S2: The derived parameters from the potentiodynamic polarization curves at pH 5 and scan rate (0.1 mV/s), in a saturated CO<sub>2</sub> environment (pH~5); Table S3: The derived parameters from the potentiodynamic polarization curves at pH 5 and scan rate (1 mV/s), in a saturated CO<sub>2</sub> environment (pH~5); Table S4: The derived parameters from the potentiodynamic polarization curves at pH 5 and scan rate (10 mV/s), in a saturated CO<sub>2</sub> environment (pH~5); Table S5: Effect of different concentrations of NaCl and scan rate on the derived values of the rate of annihilation ( $j_m$ ) and metal cation diffusivity ( $D$ ) in a saturated CO<sub>2</sub> environment (pH~5).

**Author Contributions:** Conceptualization, R.C. and H.C.; methodology, A.B.R. and A.M.M.; validation, R.C. and A.B.R.; formal analysis, A.B.R.; investigation, A.B.R. and A.M.M.; resources, N.J.A.-T.; data curation, R.C. and A.B.R.; writing—original draft preparation, A.B.R.; writing—review and

editing, R.C., H.C., A.M.M., N.H.A.-Q., A.M.A., N.J.A.-T.; visualization, M.A.M.E.-H. and J.B.; supervision, R.C. and H.C.; project administration, J.B.; funding acquisition, N.J.A.-T. All authors have read and agreed to the published version of the manuscript.

**Funding:** This research was funded by Qatar National Research Fund grant number NPRP12S-0203-190038.

**Institutional Review Board Statement:** Not applicable.

**Informed Consent Statement:** Not applicable.

**Data Availability Statement:** The data can be obtained from the authors on request.

**Acknowledgments:** The authors are thankful for the financial support from NPRP grants NPRP12S-0203-190038 from the Qatar National Research Fund (a member of Qatar Foundation). The SEM study was accomplished in the Central Laboratories unit, Qatar University.

**Conflicts of Interest:** The authors declare no conflict of interest.

## References

1. Pahlavan, S.; Moazen, S.; Taji, I.; Saffar, K.; Hamrah, M.; Moayed, M.; Beidokhti, S.M. Pitting corrosion of martensitic stainless steel in halide bearing solutions. *Corros. Sci.* **2016**, *112*, 233–240. [[CrossRef](#)]
2. Barroux, A.; Ducommun, N.; Nivet, E.; Laffont, L.; Blanc, C. Pitting corrosion of 17-4PH stainless steel manufactured by laser beam melting. *Corros. Sci.* **2020**, *169*, 108594. [[CrossRef](#)]
3. Caines, S.; Khan, F.; Shirokoff, J. Analysis of pitting corrosion on steel under insulation in marine environments. *J. Loss Prev. Process Ind.* **2013**, *26*, 1466–1483. [[CrossRef](#)]
4. Soltis, J. Passivity breakdown, pit initiation and propagation of pits in metallic materials—Review. *Corros. Sci.* **2015**, *90*, 5–22. [[CrossRef](#)]
5. Lei, X.; Feng, Y.; Zhang, J.; Fu, A.; Yin, C.; Macdonald, D.D. Impact of Reversed Austenite on the Pitting Corrosion Behavior of Super 13Cr Martensitic Stainless Steel. *Electrochim. Acta* **2016**, *191*, 640–650. [[CrossRef](#)]
6. Zhang, B.; Wang, J.; Wu, B.; Guo, X.W.; Wang, Y.J.; Chen, D.; Zhang, Y.C.; Du, K.; Oguzie, E.E.; Ma, X.L. Unmasking chloride attack on the passive film of metals. *Nat. Commun.* **2018**, *9*, 2559. [[CrossRef](#)] [[PubMed](#)]
7. Salahi, S.; Kazemipour, M.; Nasiri, A. Effects of microstructural evolution on the corrosion properties of AISI 420 martensitic stainless steel during cold rolling process. *Mater. Chem. Phys.* **2020**, *258*, 123916. [[CrossRef](#)]
8. Ge, H.-H.; Zhou, G.-D.; Wu, W.-Q. Passivation model of 316 stainless steel in simulated cooling water and the effect of sulfide on the passive film. *Appl. Surf. Sci.* **2003**, *211*, 321–334. [[CrossRef](#)]
9. Dean, M.H.; Stimming, U. The electronic properties of disordered passive films. *Corros. Sci.* **1989**, *29*, 199–211. [[CrossRef](#)]
10. Carmezim, M.; Simões, A.; Montemor, F.; Belo, M.D.C. Capacitance behaviour of passive films on ferritic and austenitic stainless steel. *Corros. Sci.* **2005**, *47*, 581–591. [[CrossRef](#)]
11. Luo, H.; Wang, X.; Dong, C.; Xiao, K.; Li, X. Effect of cold deformation on the corrosion behaviour of UNS S31803 duplex stainless steel in simulated concrete pore solution. *Corros. Sci.* **2017**, *124*, 178–192. [[CrossRef](#)]
12. Taveira, L.; Montemor, M.; Belo, M.D.C.; Ferreira, M.; Dick, L. Influence of incorporated Mo and Nb on the Mott–Schottky behaviour of anodic films formed on AISI 304L. *Corros. Sci.* **2010**, *52*, 2813–2818. [[CrossRef](#)]
13. Bojinov, M.; Fabricius, G.; Laitinen, T.; Mäkelä, K.; Saario, T.; Sundholm, G. Coupling between ionic defect structure and electronic conduction in passive films on iron, chromium and iron–chromium alloys. *Electrochim. Acta* **2000**, *45*, 2029–2048. [[CrossRef](#)]
14. Zhang, Y.; Urquidi-Macdonald, M.; Engelhardt, G.R.; Macdonald, D.D. Development of localized corrosion damage on low pressure turbine disks and blades: I. Passivity. *Electrochim. Acta* **2012**, *69*, 1–11. [[CrossRef](#)]
15. Hamadou, L.; Kadri, A.; Benbrahim, N. Impedance investigation of thermally formed oxide films on AISI 304L stainless steel. *Corros. Sci.* **2010**, *52*, 859–864. [[CrossRef](#)]
16. Bou-Saleh, Z.; Shahryari, A.; Omanovic, S. Enhancement of corrosion resistance of a biomedical grade 316LVM stainless steel by potentiodynamic cyclic polarization. *Thin Solid Films* **2007**, *515*, 4727–4737. [[CrossRef](#)]
17. Macdonald, D.D.; Biaggio, S.R.; Song, H. Steady-State Passive Films. *J. Electrochem. Soc.* **1992**, *139*, 170–177. [[CrossRef](#)]
18. Macdonald, D.D. The Point Defect Model for the Passive State. *J. Electrochem. Soc.* **1992**, *139*, 3434–3449. [[CrossRef](#)]
19. Freire, L.; Carmezim, M.; Ferreira, M.; Montemor, M. The passive behaviour of AISI 316 in alkaline media and the effect of pH: A combined electrochemical and analytical study. *Electrochim. Acta* **2009**, *55*, 6174–6181. [[CrossRef](#)]
20. Zhang, Y.; Macdonald, D.D.; Urquidi-Macdonald, M.; Engelhardt, G.R.; Dooley, R.B. Passivity breakdown on AISI Type 403 stainless steel in chloride-containing borate buffer solution. *Corros. Sci.* **2006**, *48*, 3812–3823. [[CrossRef](#)]
21. Hoar, T.; Mears, D.; Rothwell, G. The relationships between anodic passivity, brightening and pitting. *Corros. Sci.* **1965**, *5*, 279–289. [[CrossRef](#)]
22. Chao, C.Y.; Lin, L.F.; Macdonald, D.D. A Point Defect Model for Anodic Passive Films. I. *Film Growth Kinetics J. Electrochem. Soc.* **1981**, *128*, 1187–1194. [[CrossRef](#)]
23. Lin, L.F.; Chao, C.Y.; Macdonald, D.D. A Point Defect Model for Anodic Passive Films. II. *Chemical Breakdown and Pit Initiation J. Electrochem. Soc.* **1981**, *128*, 1194. [[CrossRef](#)]

24. Fischer, D.A.; Vargas, I.T.; Pizarro, G.E.; Armijo, F.; Walczak, M. The effect of scan rate on the precision of determining corrosion current by Tafel extrapolation: A numerical study on the example of pure Cu in chloride containing medium. *Electrochim. Acta* **2019**, *313*, 457–467. [[CrossRef](#)]
25. Zhang, X.; Jiang, Z.; Yao, Z.; Song, Y.; Wu, Z. Effects of scan rate on the potentiodynamic polarization curve obtained to determine the Tafel slopes and corrosion current density. *Corros. Sci.* **2009**, *51*, 581–587. [[CrossRef](#)]
26. Rizzo, R.; Baier, S.; Rogowska, M.; Ambat, R. An electrochemical and X-ray computed tomography investigation of the effect of temperature on CO<sub>2</sub> corrosion of 1Cr carbon steel. *Corros. Sci.* **2020**, *166*, 108471. [[CrossRef](#)]
27. Liu, Z.; Gao, X.; Du, L.; Li, J.; Li, P.; Yu, C.; Misra, R.; Wang, Y. Comparison of corrosion behaviour of low-alloy pipeline steel exposed to H<sub>2</sub>S/CO<sub>2</sub>-saturated brine and vapour-saturated H<sub>2</sub>S/CO<sub>2</sub> environments. *Electrochim. Acta* **2017**, *232*, 528–541. [[CrossRef](#)]
28. Hackerman, N. Effect of Temperature on Corrosion of Metals by Water. *Ind. Eng. Chem.* **1952**, *44*, 1752–1755. [[CrossRef](#)]
29. Pardo, A.; Merino, M.; Coy, A.E.; Viejo, F.; Arrabal, R.; Matykina, E. Pitting corrosion behaviour of austenitic stainless steels—Combining effects of Mn and Mo additions. *Corros. Sci.* **2008**, *50*, 1796–1806. [[CrossRef](#)]
30. Tobler, W.; Virtanen, S. Effect of Mo species on metastable pitting of Fe18Cr alloys—A current transient analysis. *Corros. Sci.* **2006**, *48*, 1585–1607. [[CrossRef](#)]
31. Frankel, G.S.; Stockert, L.; Hunkeler, F.; Boehni, H. Metastable Pitting of Stainless Steel. *Corrosion* **1987**, *43*, 429–436. [[CrossRef](#)]
32. Tian, W.; Li, S.; Du, N.; Chen, S.; Wu, Q. Effects of applied potential on stable pitting of 304 stainless steel. *Corros. Sci.* **2015**, *93*, 242–255. [[CrossRef](#)]
33. Jones, D.A. *Principles and Preventions of Corrosion*; Macmillan Publishing Company: New York, NY, USA, 1992; p. 213.
34. Yang, S.; Macdonald, D.D. Theoretical and experimental studies of the pitting of type 316L stainless steel in borate buffer solution containing nitrate ion. *Electrochim. Acta* **2007**, *52*, 1871–1879. [[CrossRef](#)]
35. Breslin, C.B.; Macdonald, D.D.; Sikora, E.; Sikora, J. Photo-inhibition of pitting corrosion on types 304 and 316 stainless steels in chloride-containing solutions. *Electrochim. Acta* **1997**, *42*, 137–144. [[CrossRef](#)]
36. Case, R.; Rincon, H.; McIntyre, D. Analysis of Pit Stability in Type 316L Stainless Steel Exposed to H<sub>2</sub>S-Saturated Dilute Chloride Solutions Above the Critical Pitting Temperature. *Corrosion* **2012**, *68*, 035004-1. [[CrossRef](#)]
37. Sun, L.; Zhao, T.; Qiu, J.; Sun, Y.; Li, K.; Zheng, H.; Jiang, Y.; Li, Y.; Li, J.; Li, W.; et al. Point defect model for passivity breakdown on hyper-duplex stainless steel 2707 in solutions containing bromide at different temperatures. *Corros. Sci.* **2021**, *194*, 109959. [[CrossRef](#)]
38. Lu, P.; Engelhardt, G.R.; Kursten, B.; Macdonald, D.D. The Kinetics of Nucleation of Metastable Pits on Metal Surfaces: The Point Defect Model and Its Optimization on Data Obtained on Stainless Steel, Carbon Steel, Iron, Aluminum and Alloy-22. *J. Electrochem. Soc.* **2016**, *163*, C156–C163. [[CrossRef](#)]
39. Simões, A.; Ferreira, M.; Lorang, G.; Belo, M.D.C. Influence of temperature on the properties of passive films formed on AISI 304 stainless steel. *Electrochim. Acta* **1991**, *36*, 315–320. [[CrossRef](#)]